Multi-modal Image Reconstruction of Electrical Impedance Tomography Using Kernel Method

Multi-modal Image Reconstruction of Electrical Impedance Tomography Using Kernel Method

Zhe Liu, *Student Member, IEEE*, Yunjie Yang, *Member, IEEE*

***Abstract*—The inverse problem of Electrical Impedance Tomography (EIT) is non-linear and severely ill-posed, resulting in relatively low image quality, which specifically, involves the aspects of structure preservation and conductivity contrast differentiation. In this paper, we report a kernel method based multi-modal EIT image reconstruction approach to tackle this challenge. The kernel method performs image-level segmentation-free information fusion and incorporates the structural information of an auxiliary high-resolution image into the EIT inversion process through the kernel matrix, which leads to an unconstrained least square problem. We describe this approach in a general way so that the high-resolution images from a variety of different imaging modalities can be adopted as the auxiliary image, if they contain sufficient structural information. In comparison with some state-of-the-art algorithms, the proposed kernel method generates superior EIT images on challenging simulation and experimental phantoms. Moreover, it presents the advantage of suppressing the interference of the existence of imaging-irrelevant objects in the auxiliary image to some extent. Simulation and experiment results also suggest the kernel method has great potential to be applied to more complicated tissue engineering applications in the future.**

***Index Terms*—Electrical Impedance Tomography, kernels, image-assisted reconstruction, multi-modal imaging**

I. INTRODUCTION

Electrical Impedance Tomography (EIT) is a widely investigated functional imaging modality that attempts to reveal the conductivity distribution of the sensing region through boundary voltage measurements [1, 2]. Attributing to its portability, non-intrusiveness, non-radiation and high temporal resolution, EIT stands out as an ideal bedside imaging candidate for real-time and long-term imaging in many biological and medical applications, such as pulmonary ventilation and perfusion imaging [3, 4], cell culture imaging [5, 6], hip surgery assistant imaging [7] and brain function imaging [8]. Especially, as the cell culture model transits from two-dimensional (2D) cell culture to three-dimensional (3D) cell culture, EIT as a suitable technique due to the mentioned advantages has been applied to 3D cultivated cell imaging and is proved as a promising approach [5, 6, 9, 10]. However, the intrinsic low spatial resolution of EIT, around 10% of the sensor diameter [2], leads to extremely low image quality and limits it to further application in this field. For example, EIT cannot reveal the size change of the cultivated cell spheroids because of the loss of structural information caused by its low spatial resolution. Therefore, techniques to improve EIT image quality is urgently desired.

In recent years, research to improve EIT image quality mainly focuses on image reconstruction algorithms. Although Sparse Bayesian Learning [11-13] offers a statistical perspective to EIT inverse problem, the dominant class of methods is still based on the regularized optimization problem. The regularization term in this type of approaches encodes certain global or local prior information to help improve EIT image quality. Reported regularizations encoding global information include sparse regularization [14-16], Total Variation (TV) regularization [17-19] and sparse representation [20]. Group Sparsity regularization provides local prior information and is also widely investigated [21, 22]. However, these methods are only based on the voltage data, i.e., single-modal image reconstruction, and the encoded prior information often comes from experience and observation, which results in limited improvement of EIT image quality.

Another idea to improve EIT image quality is to integrate other imaging modalities into EIT, which leads to dual-modal or multi-modal EIT image reconstruction. In this type of methods, the sensing area of all imaging modalities is same. However, the number of studies on the dual-modal or multi-modal EIT image reconstruction is limited although this approach has presented huge potential for the improvement of EIT image quality. Liang et al. combined EIT with ultrasound tomography (UT) and presented improved image quality due to the complement of the sensitivity distribution of the two modalities [23]. Other works on EIT-UT joint imaging also make a noticeable improvement on the resulting image quality [24, 25]. Ehrhardt et al. used parallel level sets approach to integrate the structural information in the form of edge direction from another auxiliary image into EIT image reconstruction [26] and their results display shape-preserved EIT images. In addition, Li et al. used the CT image as the auxiliary image to help EIT inversion and also presented quality improved EIT image [27]. The structural information in the CT image in the form of regularization term, i.e., Cross-Gradient regularization, is added to the optimization problem of EIT inversion to iteratively constrain the conductivity estimation.

For addressing the aforementioned challenges of EIT, i.e. lack of structural information of the imaging targets and poor

Z. Liu and Y. Yang are with the Intelligent Sensing, Analysis and Control Group, Institute for Digital Communications, School of Engineering, The University of Edinburgh, Edinburgh, UK, EH9 3JL (Corresponding author: Yunjie Yang, e-mail: y.yang@ed.ac.uk).

Manuscript received xx, 2021.

ability of differentiating different conductivity levels, in this paper, we adopt the approach of dual-modal image reconstruction. The structural information coming from another high-resolution imaging modality is integrated into EIT image reconstruction process by the kernel trick, which makes the ultimately reconstructed image contain both functional and structural information of the imaging targets. The kernel method is originated in machine learning [28] and has been successfully applied to PET image reconstruction [29, 30] with the advantages of easy implementation and effective information fusion. Using the same method in EIT, the intermediate bridging the inverse problem with the structural information of the auxiliary image is the kernel matrix, which is calculated according to the auxiliary image based on carefully defined feature vectors and a kernel, or kernel function. Then, the EIT inversion can be easily expressed as the most basic least squares problem. In the statement of the kernel method, we do not specify the high-resolution imaging modality providing auxiliary images and describe it in a general manner, which means the proposed method can be generalized to any imaging modality, e.g. CT, if this modality can offer a high-resolution image. The performance of the proposed method is comprehensively compared with single-modal algorithms, i.e., the most classical standard Tikhonov regularization based method (TReg) [31] and the state-of-the-art Structure-Aware Sparse Bayesian Learning algorithm (SA-SBL) [11], and a recently proposed dual-modal algorithm, i.e., Cross-Gradient regularization based method [27] through challenging numerical simulation and real-world experiments. Except SA-SBL, other comparative algorithms are converted to the least squares form and solved by the same optimization algorithm as that used by the kernel method to make comparison fairer. The advantages of the kernel method are summarized below:

1) Compared with given algorithms, the proposed kernel method can not only preserve the object structure in the reconstructed image but also can make a vast of improvements on the conductivity contrasts.
2) Kernel method presents a strong robustness to noise of the auxiliary image. Even in the worst situation of there are imaging-irrelevant objects, e.g. electrodes, in the auxiliary image, the kernel method can suppress the negative effect of those objects to some extent.

The structure of this paper is organized as: Section II states the principle of EIT inverse problem. Section III describes the proposed kernel method for image-assisted EIT reconstruction and a brief introduction to comparative algorithms. Section IV illustrates simulation and experimental results and makes comparison among algorithms. Finally, Section V draws the concluding remarks and discusses future work.

II. Principle of EIT Image Reconstruction

Considering a bounded, simple connected domain $\Omega \subset R^D$, $D = 2$ or 3, sixteen electrodes are attached on the boundary $\partial\Omega$ (see Fig. 1). In time-difference EIT, the aim of image reconstruction is to acquire the discrete conductivity change, denoted by the vector $\Delta\boldsymbol{\sigma} \in R^N$, within Ω between two distinct

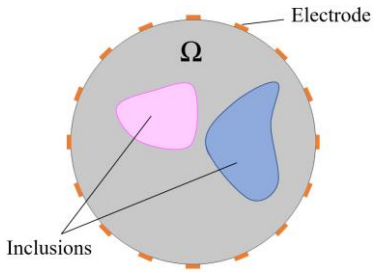

Fig. 1. Sixteen-electrode circular EIT sensor which contains two inclusions in its sensing region.

time points. The i^{th} element of $\Delta\boldsymbol{\sigma}$ denotes the conductivity change of a certain point in the sub-domain Ω_i of Ω. Sub-domains are determined by the selected inverse mesh and satisfy $\Omega = \bigcup_{i=1}^{N} \Omega_i$. The inverse mesh used in this work can refer to Fig. 4 (b), which also indicates the relationship between the position of a pixel in the mesh and that in the vector. The linearized EIT model exists to approximate the relations between the discrete conductivity changes and the induced voltage changes measured on the electrodes:

$$\mathbf{S}\Delta\boldsymbol{\sigma} = \Delta\mathbf{V} \tag{1}$$

where $\Delta\mathbf{V} \in R^M$ represents the measured voltage changes and $\mathbf{S} \in R^{M\times N}$ denotes the Jacobian matrix or sensitivity matrix, which is defined as:

$$\mathbf{S}(m^{pq}, i) = -\int_{\Omega_i} \nabla u(I^p) \nabla u(I^q) d\omega \tag{2}$$

where $\mathbf{S}(m^{pq}, i)$ denotes the sensitivity value at the $(m^{pq})^{\text{th}}$ row and i^{th} column in $\mathbf{S}$. m^{pq} represents $(m^{pq})^{\text{th}}$ measurement which corresponds the situation that the electrode pair p is set as stimulation electrodes and q is set as measurement electrodes. $\nabla u(I^p)$ and $\nabla u(I^q)$ represent the electrical potential distribution in Ω when the p^{th} and q^{th} electrode pairs are chosen as stimulation electrodes, respectively.

To estimate $\Delta\boldsymbol{\sigma}$ based on $\Delta\mathbf{V}$ and $\mathbf{S}$, a general regularization based approach can be formulated as the following penalized optimization problem, i.e.

$$\widehat{\Delta\boldsymbol{\sigma}} = \arg\min_{\Delta\boldsymbol{\sigma}} \frac{1}{2}\|\mathbf{S}\Delta\boldsymbol{\sigma} - \Delta\mathbf{V}\|^2 + \ell\Lambda(\Delta\boldsymbol{\sigma}) \tag{3}$$

where $\widehat{\Delta\boldsymbol{\sigma}}$ represents the calculated conductivity change distribution; $\|\cdot\|$ denotes the l_2 norm; $\Lambda(\cdot)$ is the regularization function, which is determined by the prior information, and $\ell \geq 0$ is the regularization factor.

III. Method

We introduce the kernel method to encode the structural information extracted from an auxiliary image obtained from a high-resolution imaging modality (e.g. CT, optical microscope) into the EIT image reconstruction process (see Fig. 2). This is inspired from the kernel-based image reconstruction methods investigated in PET image reconstruction, which have been proved effective in structure preservation [29, 30]. In this Section, we first describe the principle of EIT image reconstruction using kernel methods. Then, the practical

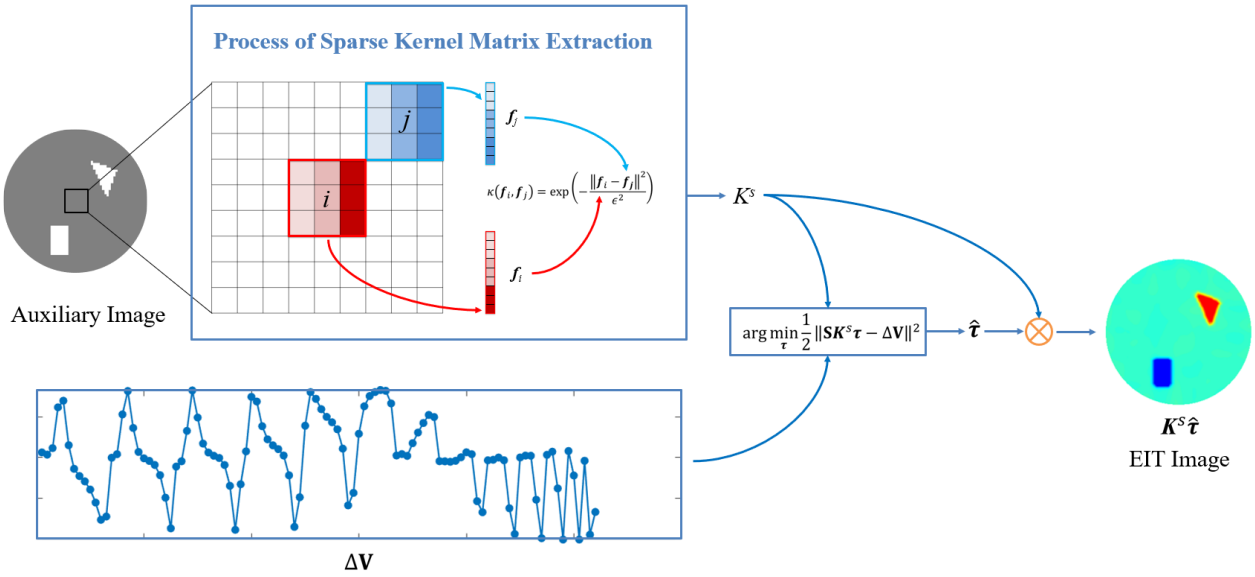

Fig. 2. The process of kernel-based EIT image reconstruction. The black mesh represents search window. The red and blue square denotes the feature window for pixel *i* and *j* respectively. ⊗ represents matrix multiplication.

definition of feature vectors, selection of kernels and proximity criteria are stated. We also briefly introduce the comparing algorithms, i.e. standard Tikhonov regularization (TReg) [31] and Cross-Gradient regularization [27].

A. Kernel-based EIT Image Reconstruction

We first predefine a set of low-dimensional feature vectors $\boldsymbol{f}_i$ at each pixel i in the expected EIT image. The set of feature vectors is the first of two mathematical objects which should be predefined in the kernel method framework [29, 30]. The second mathematical object will be described later. After the feature vectors are defined, the conductivity change at pixel i, denoted by $\Delta\boldsymbol{\sigma}_i$, can be expressed by the linear form:

$$\Delta\boldsymbol{\sigma}_i = \boldsymbol{\vartheta}^T \phi(\boldsymbol{f}_i) \tag{4}$$

where, ϕ is a mapping which transforms $\boldsymbol{f}_i$ into a very-high dimension space spanned by $\{\phi(\boldsymbol{f}_i)\}_{i=1}^N$; N is the number of pixels of the EIT image. $\boldsymbol{\vartheta}$ is a weight vector which sits in the same high-dimension space and is represented by:

$$\boldsymbol{\vartheta} = \sum_{j=1}^{N} \boldsymbol{\tau}_j \, \phi(\boldsymbol{f}_j) \tag{5}$$

where $\boldsymbol{\tau}_j$ is the coefficient for $\phi(\boldsymbol{f}_j)$. Substituting (5) into (4), the conductivity change at pixel i is written as:

$$\Delta\boldsymbol{\sigma}_i = \sum_{j=1}^{N} \boldsymbol{\tau}_j \, \phi(\boldsymbol{f}_j)^T \phi(\boldsymbol{f}_i) \triangleq \sum_{j=1}^{N} \boldsymbol{\tau}_j \, \kappa(\boldsymbol{f}_i, \boldsymbol{f}_j) \tag{6}$$

where κ is a kernel which implicitly defines ϕ. Therefore, ϕ is not required to be explicitly predefined. For simplicity, (6) can be expressed as the following matrix form:

$$\Delta\boldsymbol{\sigma} = \boldsymbol{K}\boldsymbol{\tau} \tag{7}$$

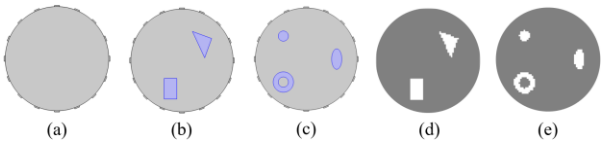

Fig. 3. Modelled (a) EIT sensor, (b) phantom 1, (c) phantom 2, (d) noiseless auxiliary image for phantom 1 and (e) noiseless auxiliary image for phantom 2.

where the element of the kernel matrix $\boldsymbol{K}$ at (i, j) is $\kappa(\boldsymbol{f}_i, \boldsymbol{f}_j)$. Under the matrix form, each column of $\boldsymbol{K}$ can be understood as a basis of $\Delta\boldsymbol{\sigma}$ and $\Delta\boldsymbol{\sigma}$ is the linear combination of all bases, i.e.

$$\Delta\boldsymbol{\sigma} = \boldsymbol{\tau}_1 \boldsymbol{K}_{:,1} + \boldsymbol{\tau}_2 \boldsymbol{K}_{:,2} + \cdots + \boldsymbol{\tau}_N \boldsymbol{K}_{:,N} \tag{8}$$

where, $\boldsymbol{K}_{:,1}$ means the first column of $\boldsymbol{K}$ and the meaning of other symbols are explained the same way. A great deal of kernels, such as polynomial kernel, can be selected to build the kernel representation of $\Delta\boldsymbol{\sigma}$. Thus, the kernel is the second mathematical object which should be predefined. It should be emphasized that the construction of the kernel matrix is based on the predefined feature vectors and the kernel function. Therefore, $\boldsymbol{K}$ is exactly the interface through which we can incorporate certain prior information into EIT image reconstruction.

In practical implementation, the full version of $\boldsymbol{K}$ for an image is usually very large, resulting in low-computational efficiency. To address this issue, the full kernel matrix $\boldsymbol{K}$ is replaced by a sparse version $\boldsymbol{K}^S$ in this work. The element of $\boldsymbol{K}^S$ at (i, j) is:

$$\boldsymbol{K}^S_{i,j} = \begin{cases} \kappa(\boldsymbol{f}_i, \boldsymbol{f}_j), & j \in kNN \text{ of } i \\ 0, & \text{otherwise} \end{cases} \tag{9}$$

where, kNN is the k nearest neighbors of the pixel i in a $d \times d$ window centered at it (named as the search window) and d should be predefined. This approach is similar to the method

adopted in the non-local mean filtering to improve computational efficiency, where the search of the similar window is conducted on the size-predefined search window rather than the entire image [32]. In addition, in Section IV, we will demonstrate the sparse kernel matrix is more suitable for EIT image reconstruction under our settings compared with the full version. During the process of $\boldsymbol{K}^S$ calculation, degree of proximity between two pixels should also be judged by a predefined proximity criterion.

Finally, substituting the equation $\Delta\boldsymbol{\sigma} = \boldsymbol{K}^S\boldsymbol{\tau}$ into (3) and discarding the regularization term in (3), the coefficient vector τ can be estimated by:

$$\hat{\boldsymbol{\tau}} = \arg\min_{\boldsymbol{\tau}} \frac{1}{2}\|\boldsymbol{S}\boldsymbol{K}^S\boldsymbol{\tau} - \Delta\mathbf{V}\|^2 \tag{10}$$

The solution of (10) naturally leads to the ultimately estimated EIT image $\widehat{\Delta\boldsymbol{\sigma}}$:

$$\widehat{\Delta\boldsymbol{\sigma}} = \boldsymbol{K}^S\hat{\boldsymbol{\tau}} \tag{11}$$

Equation (10) is a standard unconstrained least squares problem which can be effectively solved by the simple gradient descent method. The iteration equation for solving (10) is:

$$\boldsymbol{\tau}_{t+1} = \boldsymbol{\tau}_t - \alpha(\boldsymbol{K}^S)^T\mathbf{S}^T(\mathbf{S}\boldsymbol{K}^s\boldsymbol{\tau}_t - \Delta\mathbf{V}) \tag{12}$$

where, t represents iteration step and α denotes the iteration step length. We adopt early stopping as stopping critirium for our kernel-based algorithm.

B. Feature Definition, Kernel Selection, Proximity Criteria and Other Implementation Details

As stated in the last subsection, two mathematical objects, i.e., feature vectors and a kernel function, and the proximity criteria should be predefined in the kernel method framework.

In this study, we let the size of the auxiliary image equal to that of the EIT image. Thus, auxiliary image pixels and EIT image pixels coincides. Elements of the feature vector $\boldsymbol{f}_i$ are defined as the intensity values of pixels in the $y \times y$ window centered at the pixel i in the auxiliary high-resolution image. This window is called feature window and y should also be predefined. How to rearrange the elements of a feature window into a vector is illustrated in Fig. 2. The widely used radial Gaussian kernel is adopted, which is defined as:

$$\kappa(\boldsymbol{f}_i, \boldsymbol{f}_j) = \exp\left(-\frac{\|\boldsymbol{f}_i - \boldsymbol{f}_j\|^2}{\epsilon^2}\right) \tag{12}$$

where ϵ controls the sensitivity to the boundary. The *kNN* of the pixel i are in its search window and Euclidean distances between feature vectors of *kNN* and $\boldsymbol{f}_i$ are the k shortest distances among all pixels in this search window. This type of *kNN* selection method is exactly the proximity criteria.

The relationship of k and d should satisfy $k <= d^2$. Usually, we define d and y as odd number, and let $y < d$. Before $\boldsymbol{K}^S$ calculation, the feature vectors $\{\boldsymbol{f}_i\}_{i=1}^N$ are normalized by the following equation:

$$\bar{\boldsymbol{f}}_{i,z} = \frac{\boldsymbol{f}_{i,z}}{\mathrm{std}_z(\boldsymbol{f})} \tag{13}$$

where, $\boldsymbol{f}_{i,z}$ is the z^{th} element of $\boldsymbol{f}_i$ and $\mathrm{std}_z(\boldsymbol{f})$ is the standard deviation of z^{th} elements of all feature vectors. Furthermore, $\boldsymbol{K}^S$ is row normalized after its construction.

It should be noted that the kernel matrix $\boldsymbol{K}^S$ is calculated based on the auxiliary high-resolution image. Thus, $\boldsymbol{K}^S$ can be considered the container storing encoded information offered by the auxiliary image, which is exactly how the structural information of the auxiliary image associates with EIT image reconstruction.

For pixels at or near the boundary of the auxiliary image, if part of the search window of a pixel is out of the image region, pixels where the image region intersects with the feature window is set as the *kNN* candidates. Futhermore, the number of *kNN* may exceed the number of *kNN* candidates. In this case, all *kNN* candidates will be set as *kNN*. Likeswsie, at or near the boundary, part of the feature window of a pixel may be out of the image region. We apply zero padding to the auxiliary image to deal with this situation in this study.

C. Standard Tikhonov Regularization and Cross-Gradient Regularization

We implemented standard Tikhonov regularization based algorithm (TReg) [31] and Cross-Gradient regularization based algorithm [27] for comparison. The reasons of choosing TReg are twofold. First, it is the most basic algorithm in EIT image reconstruction and can be considered as the baseline of other algorithms. Second, it is the basis for Cross-Gradient method, which can be obviously reflected by (14) and (15). Compared with the estimated EIT image by TReg, one can easily find the change of EIT image when incorporating Cross-Gradient regularization term. Cross-Gradient method incorporates structural information of the auxiliary image through a penalty term, which is a different regularization approach from our method. The definitions of TReg and Cross-Gradient method are expressed by (14) and (15) respectively:

$$\widehat{\Delta\boldsymbol{\sigma}} = \arg\min_{\Delta\boldsymbol{\sigma}} \tfrac{1}{2}\|\mathbf{S}\Delta\boldsymbol{\sigma} - \Delta\mathbf{V}\|^2 + \tfrac{1}{2}\|\lambda\boldsymbol{E}\Delta\boldsymbol{\sigma}\|^2 \tag{14}$$

$$\widehat{\Delta\boldsymbol{\sigma}} = \arg\min_{\Delta\boldsymbol{\sigma}} \tfrac{1}{2}\|\boldsymbol{S}\Delta\boldsymbol{\sigma} - \Delta\mathbf{V}\|^2 + \tfrac{1}{2}\|\lambda\boldsymbol{E}\Delta\boldsymbol{\sigma}\|^2 + \tfrac{1}{2}\|\gamma G(\Delta\boldsymbol{\sigma}, \boldsymbol{\varphi})\|^2 \tag{15}$$

where $\boldsymbol{E}$ denotes the identity matrix. $\lambda \geq 0$ is the Tikhonov regularization coefficient and $\gamma \geq 0$ is the Cross-Gradient coefficient. $G(\Delta\boldsymbol{\sigma}, \boldsymbol{\varphi})$ represents the Cross-Gradient vector between the conductivity change $\Delta\boldsymbol{\sigma}$ and the pixel values of the auxiliary image $\boldsymbol{\varphi}$. $G(\Delta\boldsymbol{\sigma}, \boldsymbol{\varphi})$ can be expressed as a matrix form of $G(\Delta\boldsymbol{\sigma}, \boldsymbol{\varphi}) \triangleq \boldsymbol{G}_{\boldsymbol{\varphi}}\Delta\boldsymbol{\sigma}$; $\boldsymbol{G}_{\boldsymbol{\varphi}}$ is the transformation matrix related to $\boldsymbol{\varphi}$. Thus, both (14) and (15) can be rewritten as the form of below standard least squares, (16) and (17), respectively:

$$\widehat{\Delta\boldsymbol{\sigma}} = \arg\min_{\Delta\boldsymbol{\sigma}} \tfrac{1}{2}\left\|\begin{bmatrix}\mathbf{S}\\ \lambda\boldsymbol{E}\end{bmatrix}\Delta\boldsymbol{\sigma} - \begin{bmatrix}\Delta\mathbf{V}\\ \mathbf{0}\end{bmatrix}\right\|^2 \tag{16}$$

$$\widehat{\Delta\boldsymbol{\sigma}} = \arg\min_{\Delta\boldsymbol{\sigma}} \tfrac{1}{2}\left\|\begin{bmatrix}\mathbf{S}\\ \lambda\boldsymbol{E}\\ \gamma\boldsymbol{G}_{\boldsymbol{\varphi}}\end{bmatrix}\Delta\boldsymbol{\sigma} - \begin{bmatrix}\Delta\mathbf{V}\\ \mathbf{0}\end{bmatrix}\right\|^2 \tag{17}$$

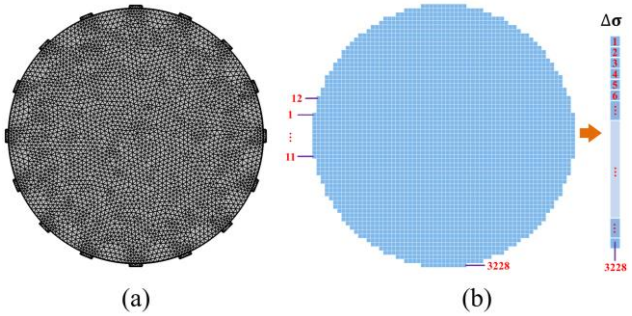

Fig. 4. (a) Forward mesh and (b) inverse mesh used in simulation. The forward mesh includes 6454 domain elements and 304 edge elements. The inverse mesh consists of 3228 elements, which makes the reconstructed EIT image a circular image internally tangent with a 64×64 square image.

Therefore, TReg and Cross-Gradient regularization based algorithm can also be solved by the same gradient descent method, which can further improve comparison fairness. Since SA-SBL is developed from another inverse framework, i.e. Bayesian perspective, it is interesting to select it to compare, but we don't provide the introduction of this algorithm.

IV. Results and Discussion

We evaluate the effectiveness and robustness of the proposed kernel method on a number of challenging numerical and experimental phantoms involving complex structures, i.e. straight lines, angles and curves, and noisy auxiliary images.

A. Synthetic Data Evaluation

1) Modelling

We modelled an EIT sensor in COMSOL Multiphysics as illustrated in Fig. 3 (a). The sensing area is circular, and its diameter is set as 15 mm. The homogeneous saline with a conductivity value of 0.05 S/m^{-1} is set as the background medium or reference medium for time difference imaging. Sixteen electrodes are evenly attached on the outer surface of the sensing area, and the electrode material is selected as Titanium whose conductivity is 7.407×10^5 S/m^{-1}. In addition, we modelled two types of complex conductivity distribution, i.e., phantom 1 to phantom 2 (see Fig. 3 (b) and Fig. 3 (c) respectively). Phantom 1 simulates two objects. The upper right one is a triangle with a conductivity values of 0.08 S/m^{-1} and the bottom left one is a rectangle with a conductivity value of 0.035 S/m^{-1}. Phantom 2 simulates three dispersed objects including a ring with a conductivity value of 0.035 S/m^{-1} (bottom left), a circle with a conductivity value of 0.015 S/m^{-1} (upper left) and an ellipse with a conductivity value of 0.025 S/m^{-1} (right) respectively. As the adjacent sensing protocol [33] is adopted in simulation and the repetitive data is eliminated according to reciprocity theory [34], a frame of voltage data consists of 104 measurements. We can acquire the voltage data by solving EIT forward problem by Finite Element Method (FEM) in COMSOL Multiphysics and the adopted forward mesh whose simplex is triangle is illustrated in Fig. 4 (a). The electrical potential of each triangular simplex is determined by the values of its vertices. On the other hand, the simplex of the mesh used in the inverse problem (see Fig. 4 (b)) is square and the conductivity value of each square simplex is the same as that of the point at the square centre. In addition to noiseless voltage data, two levels of Gaussian noise contaminated voltage data are also used, i.e., voltage data with SNR = 50 dB and voltage data with SNR = 20 dB. The SNR is defined by the below equation:

$$SNR \triangleq 10 \log_{10}\left(\frac{\|\Delta \boldsymbol{V}\|^2}{\mathcal{E}(\|\boldsymbol{\varkappa}\|^2)}\right) \tag{18}$$

where $\boldsymbol{\varkappa} \in R^M$ is the noise random variable; $\mathcal{E}(\cdot)$ is the mapping of expectation. For dual-modal algorithms, i.e. Cross-Gradient and kernel method, assisted images should also be modelled. We use the same mesh in Fig. 4 (b) to split the sensing region of the auxiliary imaging and let the intensity value of the center point of each square simplex represent the intensity value of that square, which makes the size of the auxiliary image the same as that of EIT image. In addition, we assume the auxiliary image provides accurate structure information. In real application, these images can be collected from CT imaging or optical imaging and so forth. In simulation, they are generated by assigning digit one to square simplex where there are imaging targets and assigning digit 0.5 to the background simplices. The modeled noiseless auxiliary images corresponding to sample 1 and sample 2 are shown in Fig. 3 (d) and Fig. 3 (e), respectively.

2) Parameter Settings

In simulation study, for each algorithm, different phantoms may take different parameters to make the results better, which makes the comparison under the condition of approximate limit. If not specified, all parameters use the following settings in simulation study. For results of both phantoms based on SA-SBL, the maximum iteration number is set as 5, the tolerance is selected as 1×10^{-5} and the block size is fixed as 4. The pattern coupling factor takes different values for the two phantoms, and it is chosen as 0.03 for phantom 1 and is set as

TABLE II
Image Reconstruction Comparison Based on Simulation Data

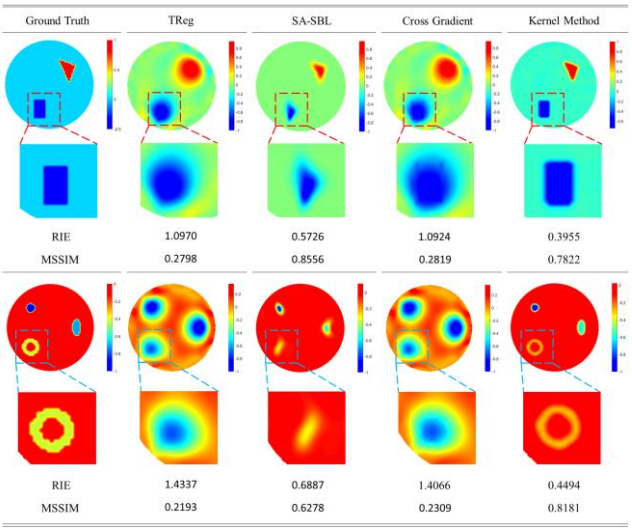

TABLE III
ASSESSMENT OF AUXILIARY IMAGE NOISE RESISTANCE ABILITY FOR KERNEL METHOD

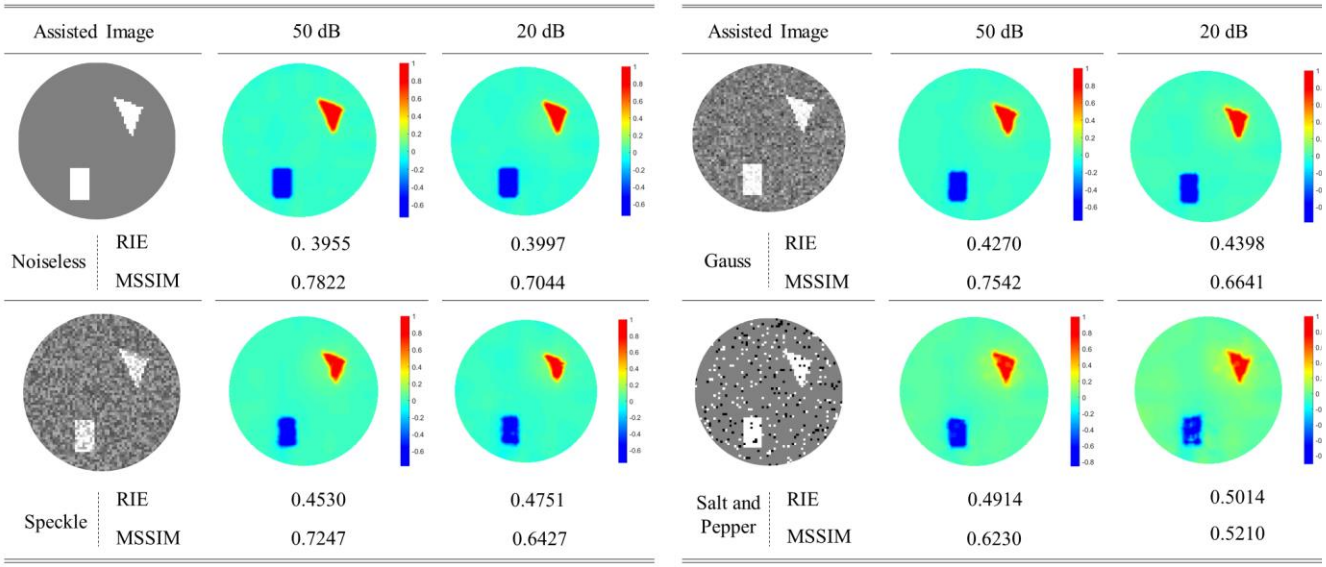

0.5 for phantom 2. According to a serial of trials, λ for both Tikhonov regularization method and Cross-Gradient regularization method is set as 0.01 for all cases and γ for Cross-Gradient regularization is set as 0.1 for all cases. For standard Tikhonov regularization and Cross-Gradient regularization, the iteration number is set as 500 and the iteration step length is set as 6 for all cases. For kernel method, the iteration number is selected as 1000 and the step length is set as 10; y is set as 3; d is set as 21; k is set as 441; and ϵ^2 is set as 20 for both phantom 1 and phantom 2.

3) Quantitative Metrics

Since we can acquire the ground truth of the conductivity distribution for simulation data, the Relative Image Error (RIE) and Mean Structural Similarity Index (MSSIM) [35] can be used to quantitatively evaluate the quality of the reconstructed image. These metrics are defined as:

$$\mathrm{RIE} = \frac{\|\Delta\boldsymbol{\sigma}_r - \Delta\boldsymbol{\sigma}_g\|}{\|\Delta\boldsymbol{\sigma}_g\|} \tag{19}$$

$$\mathrm{MSSIM} = \frac{1}{\Xi\Gamma}\sum_h\sum_b \frac{\left(2\boldsymbol{\mu}_{I_r}\boldsymbol{\mu}_{I_g} + C_1\right)\left(2\boldsymbol{\delta}_{I_rI_g} + C_2\right)}{\left(\boldsymbol{\mu}_{I_r}^2 + \boldsymbol{\mu}_{I_g}^2 + C_1\right)\left(\boldsymbol{\delta}_{I_r}^2 + \boldsymbol{\delta}_{I_g}^2 + C_2\right)} \tag{20}$$

where $\Delta\boldsymbol{\sigma}_r$ represents the reconstructed vector and $\boldsymbol{I}_r$=$\boldsymbol{I}_r(h,b)$ is the reconstructed image corresponding to it. $\Delta\boldsymbol{\sigma}_g$ denotes the ground truth vector and $\boldsymbol{I}_g = \boldsymbol{I}_g(h,b)$ is the ground truth image corresponding to it. h and b are the position indexes of an image. Ξ and Γ are the width and height of an image, respectively. $\boldsymbol{\mu}_{I_r} = \boldsymbol{\mu}_{I_r}(h,b)$, $\boldsymbol{\mu}_{I_g} = \boldsymbol{\mu}_{I_g}(h,b)$, $\boldsymbol{\delta}_{I_r} = \boldsymbol{\delta}_{I_r}(h,b)$, $\boldsymbol{\delta}_{I_g} = \boldsymbol{\delta}_{I_g}(h,b)$, and $\boldsymbol{\delta}_{I_rI_g} = \boldsymbol{\delta}_{I_rI_g}(h,b)$ are the local means, standard deviations and cross-covariance for image $\boldsymbol{I}_r$ and $\boldsymbol{I}_g$. $C_1 = (K_1L)^2$ and $C_2 = (K_2L)^2$; K_1=0.01, K_2=0.03 and L = 1 are constants [35].

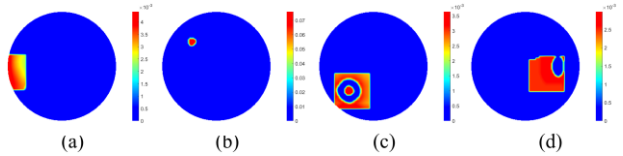

Fig. 5. Visualized images of columns in sparse kernel matrix: (a) column 10, (b) column 705, (c) column 848, and (d) column 2400.

4) Reconstruction Results and Discussion

Table II compares the performance of the kernel method with Tikhonov regularization, Cross-Gradient regularization, and Structure-aware Sparse Bayesian Learning in the case of voltage data with SNR = 50 dB and noiseless auxiliary images. For each algorithm, reconstructed EIT images, relative image error and mean structural similarity are all illustrated in this table. It is easily noticed that the TReg can predict the position of imaging targets correctly, but the structure information of targets is totally lost through the visualized images and MSSIM. Besides, the accuracy of conductivity value prediction is very low (see its RIE). The Cross-Gradient can provide some structural information which is obvious in zoomed part of images of phantom 1, i.e. straight lines of the square object can be seen. In addition, the shape of triangle object can also be identified in the image. However, the Cross-Gradient regularization is not sensitive to circular boundaries (see phantom 2 results). Moreover, our results indicate that the image quality generated by Cross-Gradient method highly relies on the image quality generated by Tikhonov regularization method, which is also indicated in original paper [27]. Therefore, the Cross-Gradient regularization can only slightly adjust the object shape, but it cannot effectively introduce a satisfactory structural information and cannot improve the accuracy of the conductivity contrast estimation. The SA-SBL recovers some object shapes well, like the triangle object in phantom 1. However, it still lost most of structural information, which can be easily found out through

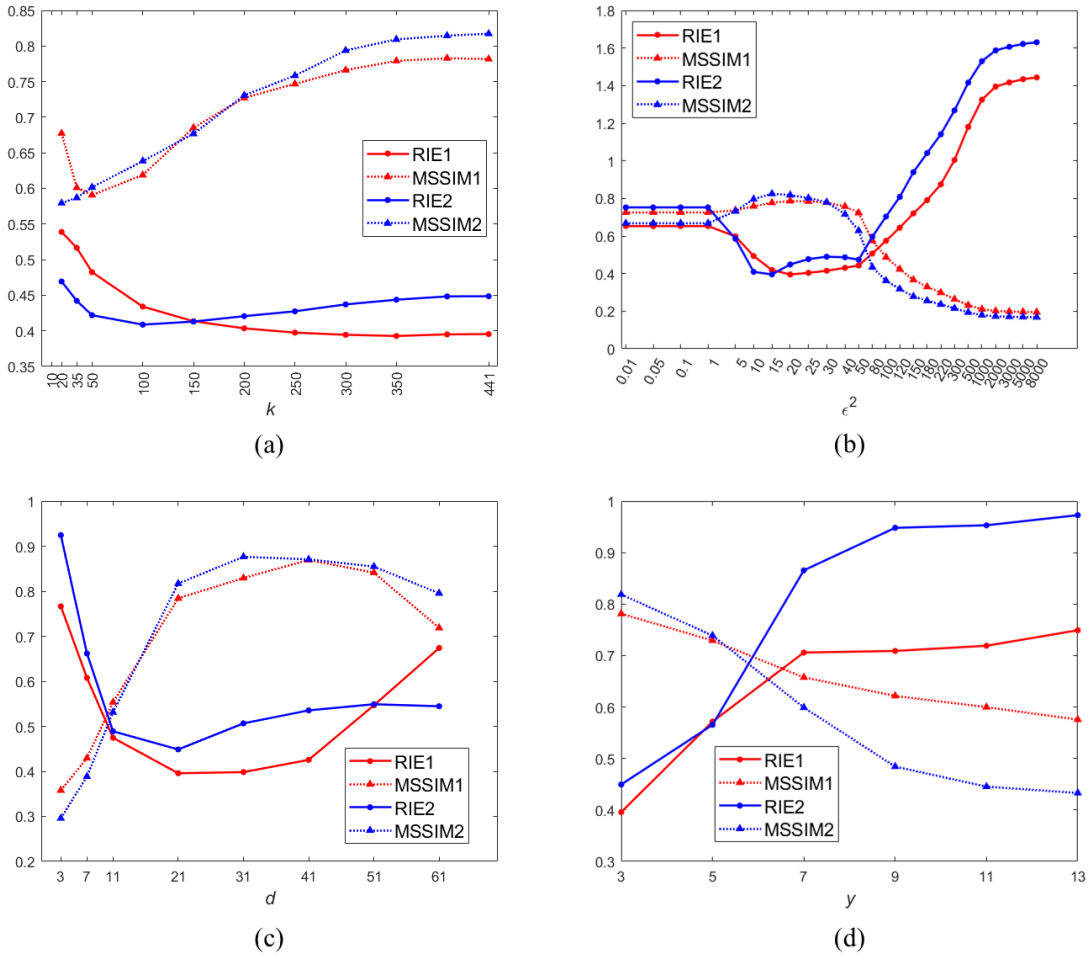

Fig. 6. Parameter setting analysis: analysis of the influence of (a) k, (b) ϵ^2, (c) d, and (d) y. RIE1 and MSSIM1 are the RIE and MSSIM for phantom 1. RIE2 and MSSIM2 represent the RIE and MSSIM for phantom 2. The two metrics share the same vertical coordinate.

reconstructed images. Though, the ability of shape recovery of SBL is not as good as that of kernel method through visualized way, the MSSIM of SA-SBL is larger than that of kernel method for phantom 1. The same thing occurs when we set the pattern coupling factor of SA-SBL as 0.03 for phantom 2, which leads the MSSIM of SA-SBL to 0.8328. This is because sparsity regularization is used in SA-SBL, which makes the background values of the image generated by SA-SBL are much lower than the background values of the image based on kernel method. If we impose zero to pixels whose absolute values are lower than 0.05 (This operation does not affect the structure of the imaging targets), the MSSIM of the kernel method result for phantom 1 will become 0.9554 while it is 0.8976 for SA-SBL; the MSSIM of the result of kernel method for phantom 2 becomes 0.9375, but it becomes 0.8589 for SA-SBL. Since the ring object is almost invisible in the image generated by SA-SBL for phantom 2 based on the pattern coupling factor of 0.03, we show the results based on such parameter of 0.5. In the former case, the RIE is 0.6973 and MSSIM is 0.8326. Therefore, we still can conclude only the proposed kernel method can predict EIT images with the most accurate position, structure, and conductivity contrasts.

Table III displays results under a considerably challenging situation, i.e., we selected phantom 1 to test the robustness of kernel method under noise-contaminated voltage data and noise-contaminated auxiliary image. We added three types of noise to the auxiliary image, i.e., Gaussian noise, Speckle noise and Salt and Pepper noise. The mean and variance of the Gaussian noise are set as zero and 0.01. The Speckle noise is based on following equation:

$$\boldsymbol{I}^*(h,b) = \boldsymbol{I}(h,b) + \boldsymbol{\iota}(h,b) \odot \boldsymbol{I}(h,b) \qquad (21)$$

where $\boldsymbol{I}^*$ is the noisy image and $\boldsymbol{I}$ is the noiseless image. $\boldsymbol{\iota}$ represents uniformly distributed random noise with mean zero and variance 0.05. $\odot$ represents Hadamard product. The Salt and Pepper noise is added with the noise density of 0.1, which means the noise will affects approximately 10% of all pixels. As shown in Table III, given a specific auxiliary image, kernel method displays a good voltage noise resistance capability (see RIE, MSSIM and EIT images). Especially, the object shape is slight affected by the voltage noise. Given a specific voltage

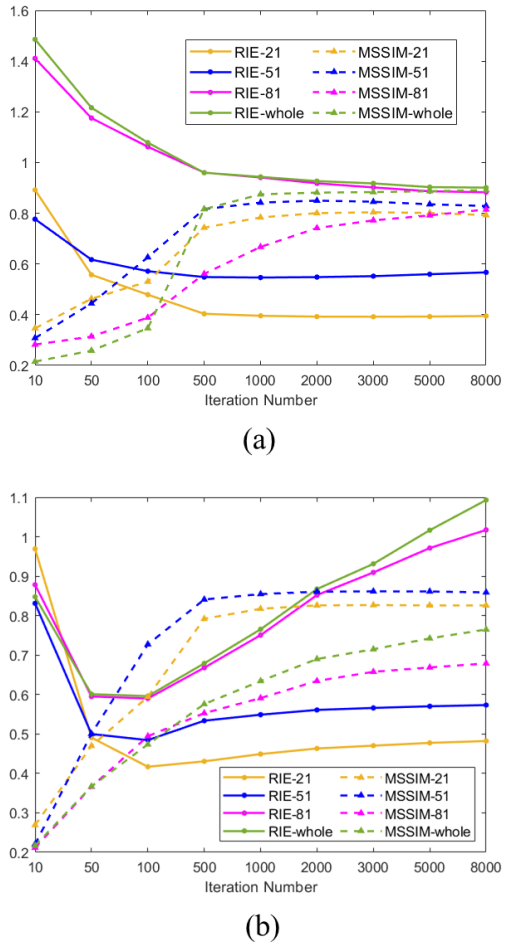

Fig. 7. Analysis of the influence of *d* based on (a) phantom 1 and (b) phantom 2. Numbers in legends means the side length of the search window, and 'whole' means the kernel matrix is calculated based on the entire image.

data, the results show that the Salt and Pepper noise can degrade the reconstructed image quality most and the Gaussian noise makes the minimal bad impact on the image quality. Besides, all types of image-noise influence the object shape not much. To sum up, the kernel method displays a satisfactory ability of both voltage noise resistance and assisted image noise resistance.

Section III-A mentions that columns of kernel matrix can be considered as the basis for EIT image. In other words, the ultimate EIT image can be seen as the linear combination of all bases. In this part of discussion, we try to explain how this combination works in a visualized way. We display four columns of the sparse kernel matrix calculated in the noiseless assisted image based on phantom 2. As shown in Fig. 5, each column represents a sub-image of the ultimate EIT image and each sub-image highlights different part of the ultimate EIT image. For example, the 848th column highlights conductivity in the bottom left area. Because pixels in ring have different structures than its peripheral region, it is not highlighted in this case. Therefore, the coefficient vector is the weights which defines the importance of each sub-images in the ultimate EIT

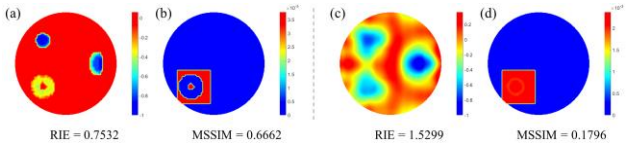

Fig. 8. Image reconstruction results based on unreasonable ϵ^2. (a) and (c) are the reconstructed images based on $\epsilon^2 = 1$ and $\epsilon^2 = 1000$,respectively. (b) and (d) are the visualizations of the 848th column of the sparse kernel matrix corresponding to (a) and (c), respectively.

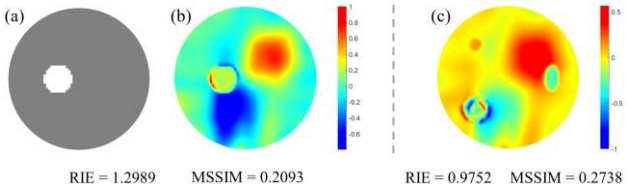

Fig. 9. Image reconstruction results of the phantom 1 based on incorrect auxiliary images. (a) is the auxiliary image corresponding to the reconstructed image (b). (c) is the reconstructed image adopting the auxiliary image in Fig. 3 (e).

image. As non-zero regions (non-blue region) in different sub-images may overlap and all sub-images will finally be added together with weights, this can reduce the influence of the noise in assisted image to some extent. Therefore, Fig. 5 also provide a qualitative explanation for why the kernel method has a auxiliary image noise resistance.

In Fig. 6, we discuss the influence of parameters k, ϵ^2, d, and y. For all analyses in this figure, the iteration number and iteration step length are fixed as 1000 and 10, respectively. We set y equal 3, d equal to 21and ϵ^2equal to 20 to analyze the influence of k. The results are shown in Fig. 6 (a), which indicates the MSSIM will be better if k increasing while the RIE has the trend of decrease. Although RIE based on phantom 2 increases when k is very large, the increment is also acceptable. Therefore, we can always choose k equals to or close to the number of pixels of the search window. We set y equal 3, d equal to 21 and k equal to 441 to analyze the influence of ϵ^2, and the results are illustrated in Fig. 6 (b). The Fig. 6 (b) presents that there is a window for the selection of ϵ^2, which indicates that the best range for ϵ^2 is around 5-50. We recommend finetuning this parameter based on specific applications. To discuss the influence of d, we fix y as 3, ϵ^2 as 20 and all pixels in the search window as the *kNN*. The results in Fig. 6 (c) demonstrate that d should not been too small or too large. It should be notated in Fig. 6 (c) that if d is much large, like 61, the MSSIM decreases much for phantom 1, which is due to the insufficient iteration number. Thus, we also study the influence of iteration number (up to 8000) based on different d. As shown in Fig. 7, we can conclude if given a large enough search window ($d \geq 21$), the MSSIM will converge to a satisfactory value. Though, MSSIM-81 and MSSIM-whole in Fig. 7 (b) are still a little low at the 8000th iteration, they also have the trend of increasing. However, the RIEs based on phantom 1 (see Fig. 7 (a)) converge while RIEs based on phantom 2 increase (see Fig. 7 (b)) with the increasing of the iteration number. If the size of the search window is not too

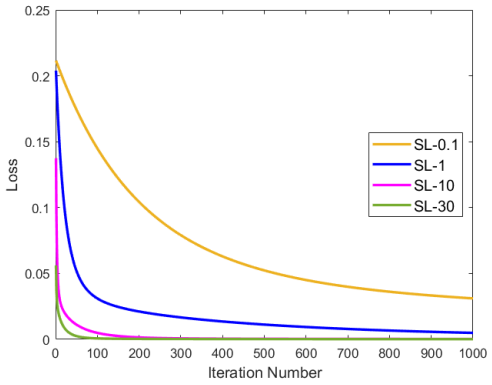

Fig. 10. Changes of objective function (loss function) in (10) with the increasing of iteration number based on different iteration step lengths (SL) and phantom 2. In legend, numbers mean the selected iteration numbers discussed.

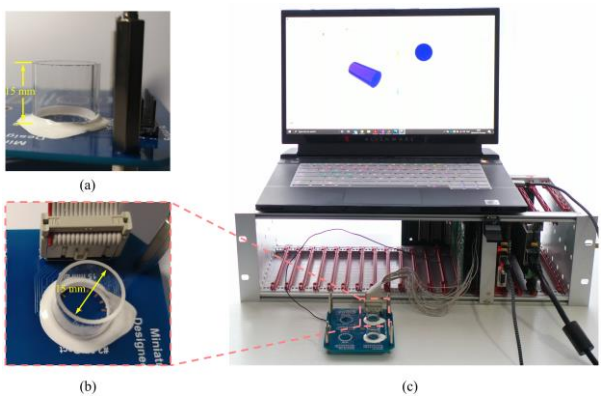

Fig. 11. (a) Side view of manufactured EIT sensor, (b) top view of manufactured EIT sensor, and (c) in-house built EIT system backend.

much big, like 21, the increment of RIEs based on phantom 2 is a little. Combing the results of Fig. 6 (c) and Fig. 7, it is easily to find that large d will impose positive impact on MSSIM while deteriorating the RIE. Therefore, the size of search window should be carefully chosen. In our study, d equal to 21 always generates satisfactory results. Fig. 6 (d) analyze the influence of y. In this case, we set d as 21, kNN as 441 and ϵ^2 as 20. From this figure, it is obvious that the size of feature window should not be set too large due to the small size of the reconstructed EIT image, i.e. a circular image inscribed in 64×64 square image. Otherwise, local information will be deteriorated because of the large feature window size. Thus, 3×3 is always recommended for the feature window size. According to the analysis, though the number of kernel method parameters, i.e. y, d, k, ϵ^2, seems a little large, only ϵ^2 should be carefully selected.

To further highlight the importance of the ϵ^2 selection, in Fig. 8, we display the reconstruction results of the phantom 2 by using kernel method with unresonable ϵ^2. Other parameters are selected the same as those in Section IV-A-2). The SNR of the voltage data is 50 dB and noise-free auxiliary image is adopted. Fig. 8 (a) is the recontructed image base on the ϵ^2 of 1 and Fig. 8 (c) is the recontructed image base on the ϵ^2 of 1000. For each situation, the 848th column of the sparse kernel matrix (Fig. 8 (b) and Fig. 8 (d)) is also displayed and it stands for why the image quality is bad. Small ϵ^2, e.g. $\epsilon^2 = 1$, is sensitive to the edge; thus the sparse kernel matrix over extract the structure. Contrarily, large ϵ^2, like $\epsilon^2 = 1000$, treats each pixel in the highlighted area of the auxiliry image same, which makes the sparse kernel matrix lack of structural information. Therefore, choosing a resonable ϵ^2 is vital in practice.

It is worth discussing the senario of the wrong auxiliary image being adopted when using kernel method and we select the phantom 1 to demonstrate. In this discussion, the voltage data of phantom 1 is added with the noise of SNR = 50 dB and the parameters for the kernel method follow the settings of Section IV-A-2). The reconstructed images in Fig. 9 (b) and Fig. 9 (c) are based on the auxiliary images in Fig. 9 (a) and Fig. 3 (e), respectively. It is noticeable that the reconstructed images are very chaotic. Though these images contain the sign of both the functional information, i.e. conductivity contrast, and structral information of the auxiliary image, the whole is totally incorrect, which can also be indicated by the RIE and MSSIM. In a word, the voltage data and the auxiliary image should match when using kernel method.

Lastly, we choose phantom 2 to study the value change of the objective function (or loss function) of the optimization problem (10) with the iteration increasing. The result is illustrated in Fig. 10. This figure demonstrtes that we can increase the interation step length to make convergence faster. In addition, as the loss decreases smoonthly, this also provides a evidance for the reliability of the early stopping criterium for our algorithm.

B. Experimental Data Evaluation

In this section, the performance of the kernel method is further validated on real data collected from experiments. The adopted miniature EIT sensor is illustrated in Fig. 11, and it is connected to the EIT system developed in the Agile Tomography Group at the University of Edinburgh [36]. The EIT sensor is used to imaging four different conductivity distributions or conductivity phantoms, and the results are illustrated in Fig. 12. The background medium for all cases is saline which conductivity is 0.05 S/m^{-1}. The Fig. 12 (a) and (b) are results of carrot tissue (length ~ 3 mm) imaging. The Fig. 12 (c) corresponds to rubber (bottom, large side length ~ 3 mm, short side length ~ 1.5 mm) and carrot tissue (upper right, large side length ~ 3.5 mm, short side length ~ 2 mm) imaging. The Fig. 12 (d) demonstrates the results of the imaging on rubber (left, diameter ~ 1.5 mm), iron (bottom, diameter ~ 2 mm), and ginger tissue (top, side length ~ 2 mm). The top surface of the iron is coated with a thin layer of white rubber to reduce the influence of surface reflection while preserving its electrical properties. The auxiliary images for Cross-Gradient and kernel method were collected from a digital camera placed over the EIT sensor. For each conductivity imaging, we adopted two types of auxiliary gray-scale images, which are shown in Fig. 12. These images are circular images inscribed in the 704×704 square region. Therefore, they cannot be directly used to construct the sparse kernel matrix. We adopted a simple way of

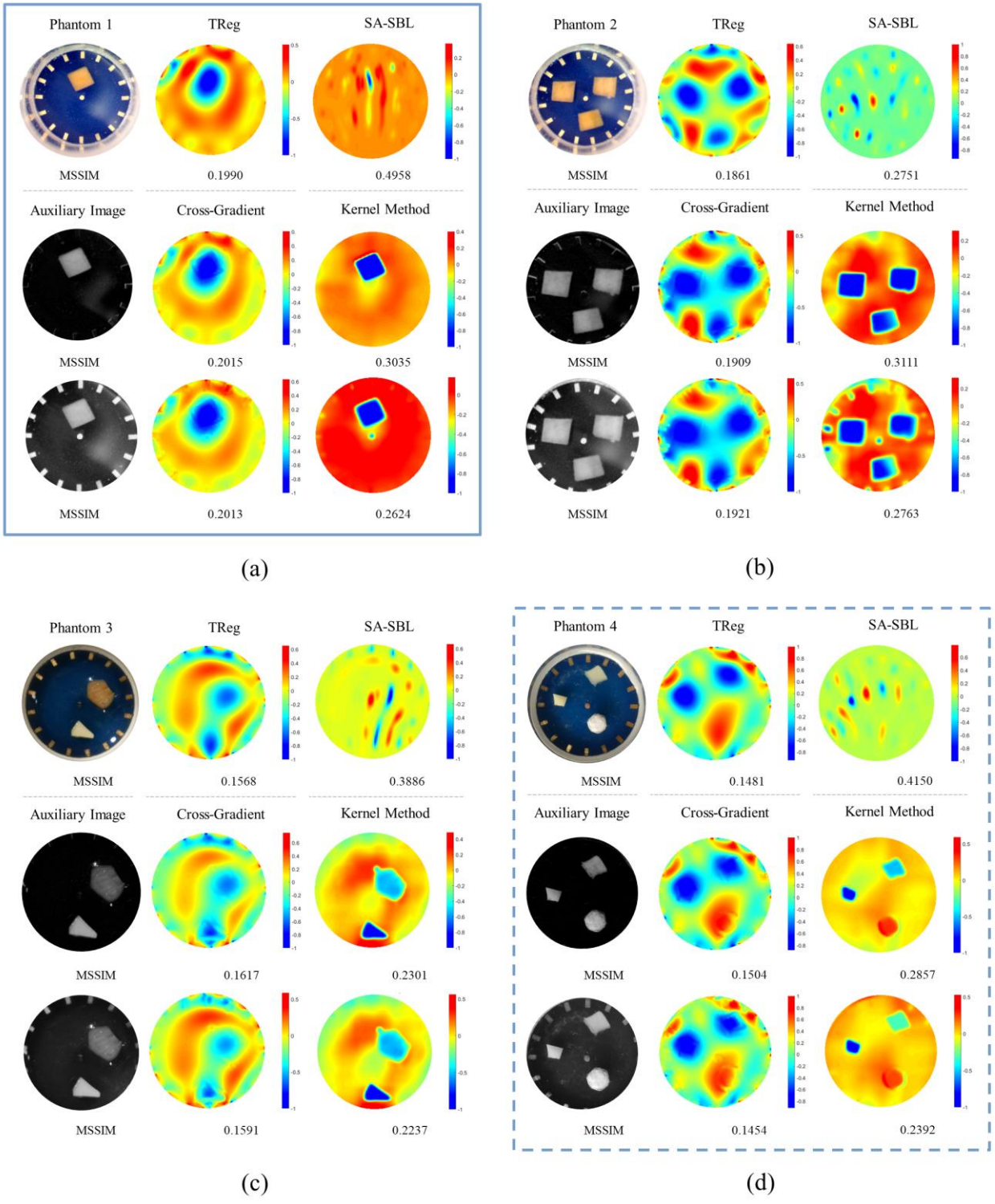

Fig. 12. Algorithm comparison based on experimental data. Blocks (a) – (d) are the results corresponding to different experimental phantoms.

down-sampling them to the EIT image size before feeding them into the kernel-based algorithm. For visualization purpose, we display the non-down-sampled auxiliary images in Fig. 12.

For the generation of the non-down-sampled auxiliary images. For each phantom, we firstly recorded an RGB microscopic image without objects as the calibration image represented by I^c. Then, an RGB microscopic image containing imaging targets is recorded and it is denoted by I^o. Due to the measurement error, we properly cropped the recorded I^o and I^c to make the imaging targets as close to the correct position as possible, which may cause the electrodes not evenly distributing along the circular boundary in the auxiliary image.

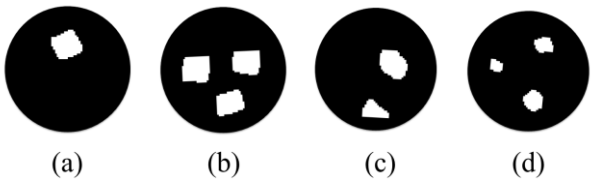

Fig. 13. Binary version of the first type of the auxiliary image. Phantom 1 - 4 correspond to (a) – (d), respectively.

TABLE IV
IMAGE SEGMENTATION RESULTS (FOR EACH PHANTOM, IMAGES FROM LEFT TO RIGHT CORRESPOND TO IMAGES FROM UP TO BOTTOM IN FIG. 12)

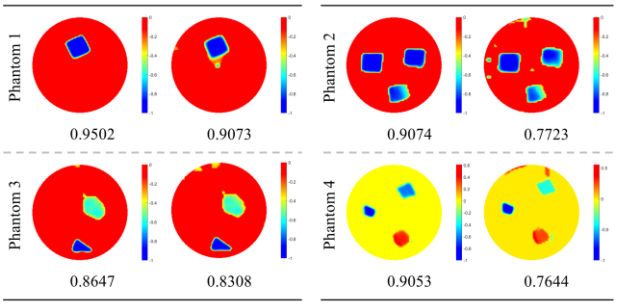

Finally, the first type of auxiliary image (upper auxiliary image for each phantom) is generated by converting $I^o - I^c$ to gray-scale image and the second type of auxiliary image (bottom auxiliary image for each phantom) is generated by directly transforming I^o to a gray-scale image.

Parameter settings for experimental data are based on a series of trails. For SA-SBL, the pattern coupling factor takes 0.03 for all phantoms and other parameters are set same as those in Section IV-A-2). For TReg and Cross-Gradient, the iteration number and iteration step length are set as 500 and 2 respectively. λ for both TReg and Cross-Gradient is set as 0.01 and γ for Cross-Gradient is selected as 1 for all cases. Except iteration number for phantom 1 and ϵ^2 for phantom 4, parameters of kernel method take same settings as in Section IV-A-2). The iteration number for phantom 1 is set as 500 for both two cases. ϵ^2 is set as 15 for the upper auxiliary image of phantom 4 and it is chosen as 7 for the bottom auxiliary image of phantom 4.

For quantitatively comparing the reconstruction results and highlighting the phantom structure in the auxiliary image, we convert the first type of auxiliary images of all phantoms into its binary version, which will be used as the reference image for MSSIM calculation later. We first normalize the auxiliary image and use the simple thresholding method to segment the auxiliary image. Pixel values lower than the threshold are set as zero and those larger than the threshold are set as one. The threshold values are selected based on trial and error and they are 0.4, 0.4, 0.4 and 0.5 for phantom 1, 2, 3 and 4 respectively. Then a post processing, i.e. open operation [37], is applied to the segmented image to adjust the boundary of the objects. For example, this operation can help remove the light reflection spot in the auxiliary image of the phantom 3. The size of the structuring element is chosen as 3×3 because we cannot make a great change to the object boundary. The final binary images are shown in Fig. 13.

The image reconstruction results are illustrated in Fig. 12. The binary images in Fig. 13 are adopted as the reference image for MSSIM calculation. In small-sale EIT imaging, the addition of imaging targets to the chamber will make noticeable variation on the height of the background medium. This means the reference conductivity changes, which causes severe artefacts in the reconstruction images based on all algorithms. For TReg, the shape of imaging targets is totally deteriorated. The image quality is also much poor for Cross-Gradient. The results are reasonable. In addition to the significant impact by the liquid height change and voltage noise, the two types of auxiliary image include not only the noise, but also imaging-irrelevant to EIT imaging like electrodes. Besides, as the discussions in Section IV-A-4), the low image quality generated by TReg can be considered as another reason contributing to the worst results of Cross-Gradient method. The SA-SBL is also powerless under this challenging experimental setup. Only the proposed kernel method presents the best performance in terms of shape preservation. Besides, it can also recover the conductivity contrasts. For example, in the imaging of ginger, rubber and iron, the conductivity of rubber is much lower than the ginger, and the iron introduces the positive conductivity change. The kernel method can differentiate the three different conductivity levels. Furthermore, it is amazing that this method can suppress the bad effect of imaging-irrelevant objects (like electrodes) appearing in the auxiliary image to some extent, which can be indicated by the background quality of the reconstructed EIT image. For all cases, it should also be noted values of MSSIM of the SA-SBL are larger than those of the kernel method. The reason we have discussed in the simulation study, and it is due to the sparsity regularization use in SA-SBL. Even though, we can also conclude the kernel method achieves the best performance on the challenging experimental data among given algorithms.

In addition, the imaging targets in the image generated by kernel method can be easily segmented from the background, which promotes post image analysis. We also use thresholding method to extract the imaging targets. For each phantom, the two reconstructed images based on different auxiliary images take the same threshold value. For phantom 1 - 3, pixel values larger than the threshold are set as zero. The threshold values are also selected based on trials and they are - 0.2, - 0.2, and - 0.3 for phantom 1, 2, and 3 respectively. For the phantom 4, the absolute values of the pixels lower than 0.22 are set as zero. The segmentation results are illustrated in Table IV. The numbers in this table are the values of the MSSIM calculated based on the segmented reconstructed images and binary images in Fig. 13. According to the results, it is verified that the low MSSIM in Fig. 12 for kernel method is mainly caused by the background noise and artefacts. Both the images and numerical metrics indicate kernel method's satisfactory ability of structure preservation once again.

V. CONCLUSIONS

In this paper, we proposed the kernel method for high-quality

EIT image reconstruction. The robustness and effectiveness of it is verified by numerical simulation and real-world experiments. Especially, the effectiveness of kernel method can be explained by a visualized way, which is very straightforward and provides an evidence of reliability when this method in real application. Future research will extend the kernel method for 3D EIT image reconstruction and combine it with other imaging modalities, e.g., OCT, to explore quantitatively monitoring of 3D cultivated cells.

REFERENCES

[1] R. H. Bayford, "Bioimpedance tomography (electrical impedance tomography)," *Annu. Rev. Biomed. Eng.,* vol. 8, pp. 63-91, 2006.

[2] P. Metherall, D. C. Barber, R. H. Smallwood, and B. H. Brown, "Three-dimensional electrical impedance tomography," *Nature,* vol. 380, no. 6574, pp. 509-512, 1996.

[3] P. Kunst, A. V. Noordegraaf, O. Hoekstra, P. Postmus, and P. De Vries, "Ventilation and perfusion imaging by electrical impedance tomography: a comparison with radionuclide scanning," *Physiological measurement,* vol. 19, no. 4, p. 481, 1998.

[4] D. Nguyen, C. Jin, A. Thiagalingam, and A. McEwan, "A review on electrical impedance tomography for pulmonary perfusion imaging," *Physiological measurement,* vol. 33, no. 5, p. 695, 2012.

[5] H. Wu, Y. Yang, P. O. Bagnaninchi, and J. Jia, "Electrical impedance tomography for real-time and label-free cellular viability assays of 3D tumour spheroids," *Analyst,* vol. 143, no. 17, pp. 4189-4198, 2018.

[6] Y. Yang, J. Jia, S. Smith, N. Jamil, W. Gamal, and P.-O. Bagnaninchi, "A miniature electrical impedance tomography sensor and 3-D image reconstruction for cell imaging," *IEEE Sensors Journal,* vol. 17, no. 2, pp. 514-523, 2016.

[7] Z. Ren and W. Q. Yang, "Development of a navigation tool for revision total hip surgery based on electrical impedance tomography," *IEEE Transactions on Instrumentation and Measurement,* vol. 65, no. 12, pp. 2748-2757, 2016.

[8] D. S. Holder, *Electrical impedance tomography: methods, history and applications*. CRC Press, 2004.

[9] Y. Yang, H. Wu, J. Jia, and P.-O. Bagnaninchi, "Scaffold-based 3-D cell culture imaging using a miniature electrical impedance tomography sensor," *IEEE Sensors Journal,* vol. 19, no. 20, pp. 9071-9080, 2019.

[10] H. Wu, W. Zhou, Y. Yang, J. Jia, and P. Bagnaninchi, "Exploring the potential of electrical impedance tomography for tissue engineering applications," *Materials,* vol. 11, no. 6, p. 930, 2018.

[11] S. Liu, J. Jia, Y. D. Zhang, and Y. Yang, "Image reconstruction in electrical impedance tomography based on structure-aware sparse Bayesian learning," *IEEE transactions on medical imaging,* vol. 37, no. 9, pp. 2090-2102, 2018.

[12] S. Liu, H. Wu, Y. Huang, Y. Yang, and J. Jia, "Accelerated structure-aware sparse Bayesian learning for three-dimensional electrical impedance tomography," *IEEE Transactions on Industrial Informatics,* vol. 15, no. 9, pp. 5033-5041, 2019.

[13] S. Liu, Y. Huang, H. Wu, C. Tan, and J. Jia, "Efficient multitask structure-aware sparse bayesian learning for frequency-difference electrical impedance tomography," *IEEE Transactions on Industrial Informatics,* vol. 17, no. 1, pp. 463-472, 2020.

[14] J. Li, S. Yue, M. Ding, Z. Cui, and H. Wang, "Adaptive Lp Regularization for Electrical Impedance Tomography," *IEEE Sensors Journal,* vol. 19, no. 24, pp. 12297-12305, 2019.

[15] Y. Shi, Y. Wu, M. Wang, Z. Tian, X. Kong, and X. He, "Sparse image reconstruction of intracerebral hemorrhage with electrical impedance tomography," *Journal of Medical Imaging,* vol. 8, no. 1, p. 014501, 2021.

[16] J. Wang, "Non-convex ℓ p regularization for sparse reconstruction of electrical impedance tomography," *Inverse Problems in Science and Engineering,* pp. 1-22, 2020.

[17] A. Borsic, B. M. Graham, A. Adler, and W. R. Lionheart, "In vivo impedance imaging with total variation regularization," *IEEE transactions on medical imaging,* vol. 29, no. 1, pp. 44-54, 2009.

[18] B. Gong, B. Schullcke, S. Krueger-Ziolek, F. Zhang, U. Mueller-Lisse, and K. Moeller, "Higher order total variation regularization for EIT reconstruction," *Medical & biological engineering & computing,* vol. 56, no. 8, pp. 1367-1378, 2018.

[19] J. Liu, L. Lin, W. Zhang, and G. Li, "A novel combined regularization algorithm of total variation and Tikhonov regularization for open electrical impedance tomography," *Physiological measurement,* vol. 34, no. 7, p. 823, 2013.

[20] J. Ye, H. Wang, and W. Yang, "Image reconstruction for electrical capacitance tomography based on sparse representation," *IEEE Transactions on Instrumentation and Measurement,* vol. 64, no. 1, pp. 89-102, 2014.

[21] Y. Yang and J. Jia, "An image reconstruction algorithm for electrical impedance tomography using adaptive group sparsity constraint," *IEEE Transactions on Instrumentation and Measurement,* vol. 66, no. 9, pp. 2295-2305, 2017.

[22] Y. Yang, H. Wu, and J. Jia, "Image reconstruction for electrical impedance tomography using enhanced adaptive group sparsity with total variation," *IEEE Sensors Journal,* vol. 17, no. 17, pp. 5589-5598, 2017.

[23] G. Liang, S. Ren, S. Zhao, and F. Dong, "A Lagrange-Newton method for EIT/UT dual-modality image reconstruction," *Sensors,* vol. 19, no. 9, p. 1966, 2019.

[24] G. Liang, S. Ren, and F. Dong, "An adaptive local weighted image reconstruction algorithm for EIT/UTT dual-modality imaging," in *2017 IEEE International Instrumentation and Measurement Technology Conference (I2MTC)*, 2017: IEEE, pp. 1-6.

[25] H. Liu, S. Zhao, C. Tan, and F. Dong, "A bilateral constrained image reconstruction method using electrical impedance tomography and ultrasonic measurement," *IEEE Sensors Journal,* vol. 19, no. 21, pp. 9883-9895, 2019.

[26] V. Kolehmainen, M. J. Ehrhardt, and S. R. Arridge, "Incorporating structural prior information and sparsity into EIT using parallel level sets," *Inverse Problems & Imaging,* vol. 13, no. 2, p. 285, 2019.

[27] Z. Li, J. Zhang, D. Liu, and J. Du, "CT image-guided electrical impedance tomography for medical imaging," *IEEE transactions on medical imaging,* vol. 39, no. 6, pp. 1822-1832, 2019.

[28] T. Hofmann, B. Schölkopf, and A. J. Smola, "Kernel methods in machine learning," *The annals of statistics,* pp. 1171-1220, 2008.

[29] W. Hutchcroft, G. Wang, K. T. Chen, C. Catana, and J. Qi, "Anatomically-aided PET reconstruction using the kernel method," *Physics in Medicine & Biology,* vol. 61, no. 18, p. 6668, 2016.

[30] G. Wang and J. Qi, "PET image reconstruction using kernel method," *IEEE transactions on medical imaging,* vol. 34, no. 1, pp. 61-71, 2014.

[31] M. Vauhkonen, D. Vadasz, P. A. Karjalainen, E. Somersalo, and J. P. Kaipio, "Tikhonov regularization and prior information in electrical impedance tomography," *IEEE transactions on medical imaging,* vol. 17, no. 2, pp. 285-293, 1998.

[32] A. Buades, B. Coll, and J.-M. Morel, "A non-local algorithm for image denoising," in *2005 IEEE Computer Society Conference on Computer Vision and Pattern Recognition (CVPR'05)*, 2005, vol. 2: IEEE, pp. 60-65.

[33] B. H. Brown and A. D. Seagar, "The Sheffield data collection system," *Clinical Physics and Physiological Measurement,* vol. 8, no. 4A, p. 91, 1987.

[34] D. B. Geselowitz, "An application of electrocardiographic lead theory to impedance plethysmography," *IEEE Transactions on biomedical Engineering,* no. 1, pp. 38-41, 1971.

[35] Z. Wang, A. C. Bovik, H. R. Sheikh, and E. P. Simoncelli, "Image quality assessment: from error visibility to structural similarity," *IEEE transactions on image processing,* vol. 13, no. 4, pp. 600-612, 2004.

[36] Y. Yang and J. Jia, "A multi-frequency electrical impedance tomography system for real-time 2D and 3D imaging," *Review of Scientific Instruments,* vol. 88, no. 8, p. 085110, 2017.

[37] R. C. Gonzalez and P. Wintz, "Digital image processing(Book)," *Reading, Mass., Addison-Wesley Publishing Co., Inc.(Applied Mathematics and Computation,* no. 13, p. 451, 1977.